crystals

MDPI

Article

Hot Deformation Behavior and Microstructure Evolution of GTD222 Nickel-Based Superalloy

Zhiheng Zhu [1], Chunhua Xiang [2], Guangyu Wang [2], Cunqiang Ma [2], Mingpan Wan [1,*] and Min Lei [1,*]

[1] College of Materials and Metallurgy, Guizhou University, Guiyang 550025, China
[2] Guizhou Aviation Technical Development Co., Ltd., Guiyang 550081, China
* Correspondence: mpwan@gzu.edu.cn (M.W.); amin_am@163.com (M.L.)

Abstract

Hot workability of GTD222 nickel-based superalloy was examined by isothermal compression over 1010–1090 °C and 0.01–10 s^{-1} to a true strain of 1.2. The flow resistance increased as the temperature decreased or the strain rate increased. The measured curves were corrected for interfacial friction and adiabatic heating before constitutive analysis. A peak-stress relation and a strain-compensated Arrhenius model were then established; for the calibration dataset, the latter gave a correlation coefficient (R) of 0.978 and an average absolute relative error (AARE) of 6.89%. Processing maps derived from the dynamic materials model (DMM) and Prasad's instability criterion at true strains of 0.3, 0.6, 0.9, and 1.2, together with microstructural evidence, delineated 1070–1090 °C and 0.01–0.1 s^{-1} as a favorable hot-working domain. Electron backscatter diffraction (EBSD) and transmission electron microscopy (TEM) revealed that the dynamic recrystallization (DRX) fraction did not change monotonically with either temperature or strain rate, although the recrystallized grains became coarser with increasing temperature. At 1090 °C, the DRX fraction fell to 46.13% at 1 s^{-1} and recovered to 76.39% at 10 s^{-1}, plausibly reflecting the competing influences of deformation time, stored deformation energy, and adiabatic heating. Grain-boundary bulging, serration, and necklace-like recrystallized grains indicate dominant discontinuous dynamic recrystallization (DDRX), whereas intragranular orientation gradients, cumulative misorientation, medium-angle grain-boundary development, and fine intragranular grains support a supplementary contribution from continuous dynamic recrystallization (CDRX).

Keywords: GTD222 nickel-based superalloy; hot deformation; microstructural evolution; dynamic recrystallization

Check for updates

Academic Editor: Alla S. Sologubenko

Received: 24 August 2026
Revised: 17 September 2026
Accepted: 29 September 2026
Published: 30 September 2026

Copyright: © 2026 by the authors. Licensee MDPI, Basel, Switzerland. This article is an open access article distributed under the terms and conditions of the Creative Commons Attribution (CC BY) license.

1. Introduction

Components used in the hot sections of aero-engines and stationary gas turbines must retain mechanical strength while resisting creep, oxidation, and microstructural degradation at elevated temperatures. Nickel-based superalloys satisfy this combination of requirements and are therefore widely used in such environments [1,2]. GTD222 is a γ′-strengthened alloy designed for high-temperature service [3]. Its solid-solution and precipitation strengthening improve elevated-temperature stability, but they also raise the resistance to hot deformation and restrict the available processing range. Establishing the effects of temperature and strain rate on the flow response of GTD222 is thus important for designing reliable forging and thermomechanical-processing schedules.

During hot deformation, the face-centered cubic γ matrix and relatively low stacking-fault energy of nickel-based superalloys tend to limit recovery and promote DRX [4]. The resulting flow response reflects competition among work hardening, dynamic recovery (DRV), and DRX [5–7]. Tan et al. [8] associated grain refinement in IN718 mainly with DDRX through grain-boundary bulging, while CDRX played a secondary role. Song et al. [9] reported a transition from DDRX to a mixed DDRX/CDRX/DRV response in an as-cast nickel-based superalloy, and Liu et al. [10] observed increasingly pronounced CDRX in GH5188 above 1130 °C. A study on 7055 aluminum alloy by Liu et al. [11] also linked intragranular recrystallization to subgrain evolution, whereas Huang et al. [12] showed in a Ni–W–Cr superalloy that pre-existing dislocations and grain-boundary irregularities can facilitate CDRX-related substructure development.

Constitutive descriptions and processing maps provide complementary routes for quantifying flow behavior and assessing hot workability [13–16]. For GH690, Lin et al. [15] represented the flow response with a hyperbolic-sine Arrhenius relation, while Lin et al. [17] developed a physically based formulation for nickel-based superalloys. Processing-map studies have likewise reported distinct workable domains. Zhong et al. [13] identified 1010–1075 °C/0.01–1 s^{-1} and 1075–1150 °C/0.03–1 s^{-1} for GH4738, whereas Jiao et al. [18] reported favorable conditions at 1000 °C/0.01 s^{-1} and 1050–1100 °C/0.01–0.1 s^{-1} for GH4169. A recent review further emphasized that constitutive modeling, processing-map analysis, and microstructural evidence should be interpreted together when selecting thermomechanical-processing conditions for superalloys [19].

Accordingly, the present work examined the hot-deformation response and microstructural evolution of forged GTD222 over a range of temperatures and strain rates. Flow curves corrected for friction and deformation heating were used to establish peak-stress and strain-compensated Arrhenius relations. Strain-dependent processing maps were then combined with optical microscopy (OM), EBSD, and TEM observations to evaluate hot workability and to interpret the DRX mechanisms. The resulting correlations provide a basis for selecting practical thermomechanical-processing conditions for GTD222.

2. Materials and Experiments

Forged GTD222 nickel-based superalloy was used as the starting material in this study. The nominal chemical composition listed in Table 1 was determined from the composition ranges specified by the material supplier. Cylindrical specimens with a diameter of 8 mm and a height of 12 mm were prepared by wire electrical discharge machining. Hot-compression tests were conducted on a Gleeble 3800 (Dynamic Systems Inc., Poestenkill, NY, USA) thermomechanical simulator at deformation temperatures of 1010, 1030, 1050, 1070, and 1090 °C and strain rates of 0.01, 0.1, 1, and 10 s^{-1}. All specimens were compressed to a true strain of 1.2, corresponding to a height reduction of approximately 70%. To reduce interfacial friction and suppress nonuniform deformation, 0.1 mm thick tantalum foils coated with a high-temperature lubricant were placed between the specimen ends and the anvils. The thermal schedule is illustrated in Figure 1a. Before deformation, each specimen was heated from room temperature to 1200 °C at 10 °C s^{-1} and held for 120 s to improve temperature uniformity throughout the specimen. The temperature was then decreased to the prescribed deformation temperature at the same rate and maintained for 60 s before compression. Isothermal compression was subsequently performed at the selected strain rate, and the specimen was immediately water-quenched upon reaching the target strain to preserve, as closely as possible, the deformation-end microstructure.

Table 1. Nominal chemical composition of GTD222 alloy (wt%).

Element	C	Cr	Co	W	Nb	Al	Ti	Ni
Wt%	0.1	22.5	19	2	0.75	1.26	2.2	Bal.

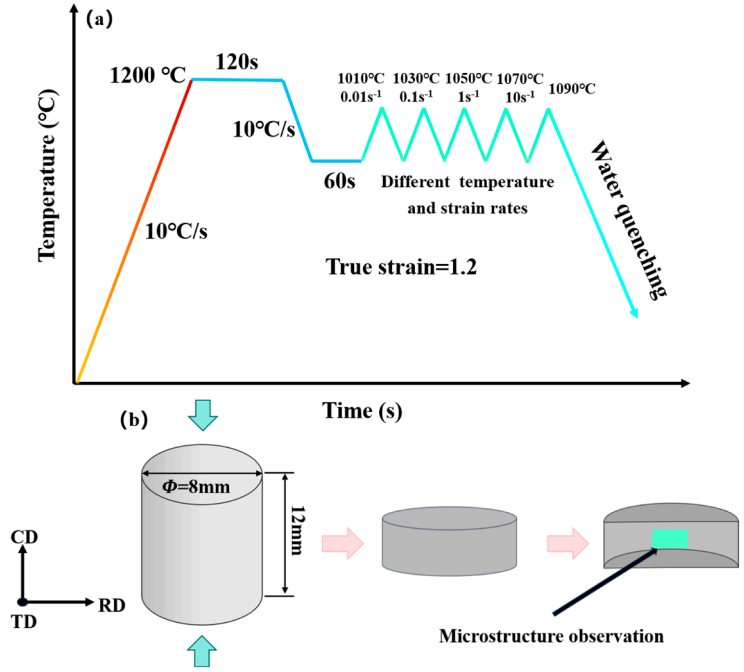

Figure 1. (**a**) Hot compression process, (**b**) sample specifications and sampling observation area. CD, RD, and TD denote the compression direction, radial direction, and tangential direction, respectively.

Microstructural characterization was carried out on longitudinal sections through the center of the compressed specimens. The OM and EBSD observation areas were selected from the central region indicated in Figure 1b, and TEM samples were taken from the corresponding region. Metallographic specimens were ground, polished, and etched in a solution containing 10 g $CuCl_2$, 50 mL HCl, and 100 mL C_2H_5OH before OM examination. For EBSD analysis, the polished surfaces were further ion-milled using a Leica RES101 (Leica Microsystems, Wetzlar, Germany) at 6.5 kV. Orientation data were acquired with an Oxford Instruments NordlysMax3 (Oxford Instruments, Abingdon, UK) detector at a step size of 0.45 μm and processed using Channel 5 (Oxford Instruments, Abingdon, UK) and AZtecCrystal (version 5.1, Oxford Instruments, Abingdon, UK). Grain orientation spread (GOS), defined as the mean misorientation between the measured orientations within a grain and its mean orientation, was used to distinguish recrystallized from deformed grains; grains with GOS $\leq 2^\circ$ were classified as recrystallized [13,20]. TEM foils were prepared by mechanical thinning followed by ion milling using a Gatan 695 system (Gatan, Inc., Pleasanton, CA, USA), and observations were performed on an FEI Talos F200X microscope (FEI Company, Hillsboro, OR, USA) operated at 200 kV.

3. Results

3.1. Initial Microstructure

Figure 2 summarizes the as-forged microstructure of the GTD222 alloy prior to the Gleeble thermal cycle. The optical micrograph in Figure 2a shows predominantly polygonal and near-equiaxed grains containing linear intragranular features consistent with annealing twins. Analysis of the EBSD inverse pole figure (IPF) data gives an average grain size of approximately 23.12 μm, with the corresponding grain-size distribution shown in Figure 2b.

According to the grain-boundary statistics in Figure 2c, low-angle grain boundaries (LAGBs, 2–15°) account for only 6.52% of the total boundary population, whereas high-angle grain boundaries (HAGBs, >15°) constitute 93.5%. Meanwhile, the dispersed crystallographic orientations in the IPF map indicate no pronounced initial preferred orientation. Overall, the as-forged GTD222 alloy is characterized by a predominantly near-equiaxed grain structure, a boundary population dominated by HAGBs, and numerous twin-like intragranular features.

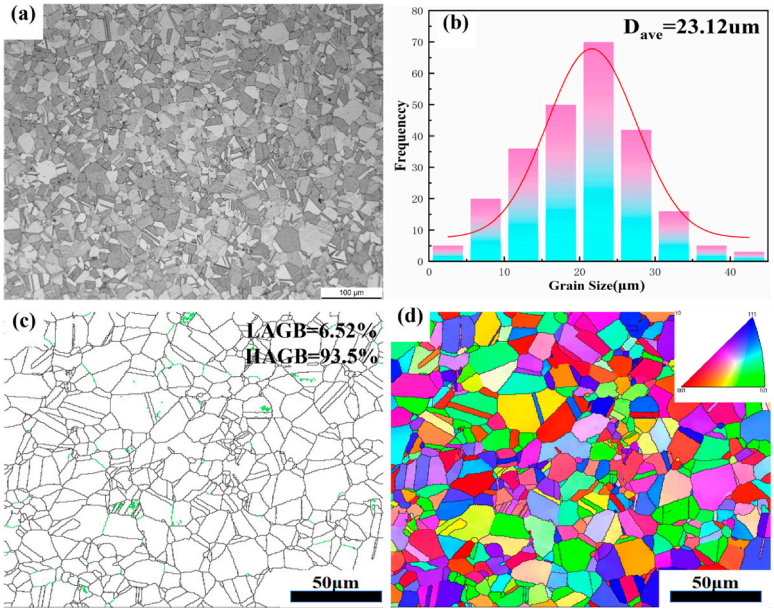

Figure 2. Initial microstructure of the GTD222 nickel-based superalloy: (**a**) OM map; (**b**) grain-size distribution; (**c**) GB map; (**d**) IPF map.

3.2. Hot Deformation Behavior

Barreling caused by friction at the specimen–anvil interfaces can increase the apparent flow stress during compression. The measured flow curves were therefore corrected using the procedure proposed by Ebrahimi et al. [21]:

$$\sigma_f = \frac{\sigma}{1 + \left(\frac{2}{3\sqrt{3}}\right) f \left(\frac{r_0}{h_0}\right) \exp\left(\frac{3\varepsilon}{2}\right)} \quad (1)$$

In Equation (1), σ_f denotes the flow stress after friction correction, whereas σ represents the measured flow stress. The parameter f is the friction correction factor, and r_0 and h_0 correspond to the initial specimen radius and height, respectively. Following the Ebrahimi approach, f is determined from the geometry of the deformed specimen instead of being assigned as a constant [21]:

$$f = \frac{\left(\frac{r}{h}\right) b}{\left(\frac{4}{\sqrt{3}}\right) - \left(\frac{2b}{3\sqrt{3}}\right)} \quad (2)$$

The parameter b in Equation (2) quantifies barreling, and r and h are the average radius and height after deformation. The geometric terms required to evaluate b were determined using Equations (3) and (4):

$$b = \frac{\Delta r}{r} \frac{h}{\Delta h} \quad (3)$$

$$r = r_0 \sqrt{\frac{h_0}{h}} \quad (4)$$

Here, Δh denotes the decrease in specimen height, whereas Δr is the difference between the maximum radius and the radius at the specimen end. Because direct measurement of the end radius is difficult, the compressed profile was represented by a circular arc and the required radius was calculated from Equation (5):

$$r_{\mathrm{T}} = \sqrt{3\frac{h_0}{h}r_0^2 - 2r_{\mathrm{M}}^2} \tag{5}$$

In Equation (5), r_T and r_M are the top and maximum radii of the compressed specimen. The measured dimensions were inserted into Equations (1)–(5) to obtain the friction-corrected stress values.

Deformation heating becomes relevant when the imposed strain rate is high because plastic work is converted to heat more rapidly than it can be removed. At strain rates of 1 s^{-1} and above, this effect can make the specimen interior hotter than the surface temperature recorded by the thermocouple. The associated temperature increment was estimated from Equation (6) [22]:

$$\Delta T = \frac{0.95\eta\int_0^{\varepsilon}\sigma d\varepsilon}{\rho c} \tag{6}$$

In Equation (6), ΔT is the deformation-induced temperature increase, ρ is density, c is specific heat capacity, and η is the adiabatic coefficient. Following Ref. [23], η was set to 0 below 0.001 s^{-1} and to 0.95 above 1 s^{-1}, with intermediate values evaluated from Equation (7). The temperature-dependent density and specific heat values used for GTD222 are summarized in Table 2:

$$\eta = 0.316\log(\dot{\varepsilon}) + 0.95 \tag{7}$$

Table 2. Physical properties of GTD222 alloy.

Temperature (°C)	Density (g/cm^3)	Specific Heat (J·g^{-1}·K^{-1})
1010	8.0309	0.60406
1030	8.02084	0.60853
1050	8.01072	0.61307
1070	8.00054	0.61768
1090	7.99029	0.62237

The change in flow stress associated with the calculated temperature rise was estimated using the relation proposed by Devadas [24]:

$$\Delta\sigma = \frac{Q}{n\alpha \mathrm{R}}\left(\frac{1}{T} - \frac{1}{T+\Delta T}\right) \tag{8}$$

Equation (8) uses the stress correction $\Delta\sigma$ together with the hot-deformation activation energy Q, gas constant R, stress exponent n, material parameter α, and absolute temperature T. The Q, n, and α values required only for this heating correction were obtained from the Arrhenius-type expression in Equation (9) [25]:

$$\dot{\varepsilon} = A\left[\sinh(\alpha\sigma_p)\right]^n \exp\left(-\frac{Q}{\mathrm{RT}}\right) \tag{9}$$

Linearizing Equation (9) with the uncorrected peak stresses yielded n = 3.9, α = 0.00375 MPa^{-1}, and Q = 4.539 × 10^5 J mol^{-1} (≈453.9 kJ mol^{-1}). These values were used solely to calculate the adiabatic-heating correction and were not carried forward as the final constitutive parameters.

Figure 3 presents the experimental flow curves together with those corrected for friction and adiabatic heating. At the onset of deformation, the stress increases rapidly because dislocation accumulation predominates over dynamic softening. With further straining, the rate of stress increase gradually diminishes, indicating that thermally activated restoration progressively counterbalances strain hardening [26]. Depending on the deformation condition, the subsequent flow response may exhibit post-peak softening, a nearly steady stage, or renewed hardening. Deformation temperature and strain rate exert opposite influences on the flow resistance. At a given strain rate, increasing the temperature facilitates diffusion, dislocation glide and climb, recovery, and grain-boundary migration, thereby reducing both the flow stress and peak stress. Conversely, at a fixed temperature, increasing the strain rate leaves less time for these restoration processes and promotes dislocation accumulation, resulting in higher stresses [27]. Deformation heating may further influence the highest-rate tests; consequently, the corrected curves were used for constitutive analysis. Overall, GTD222 flow behavior reflects the evolving balance between strain hardening and temperature- and rate-dependent restoration.

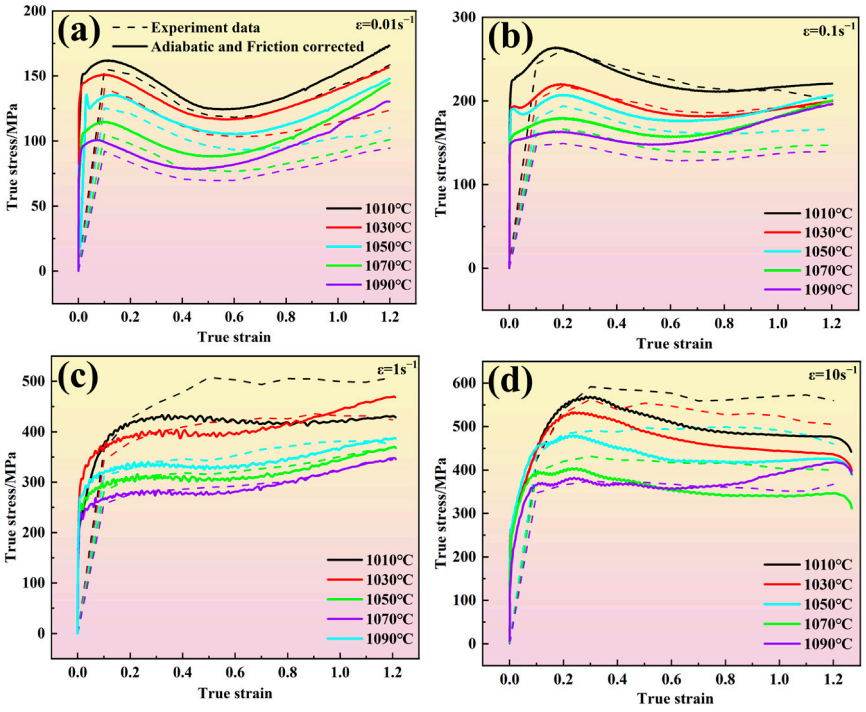

Figure 3. Experimental and corrected true stress–strain curves of the GTD222 alloy at strain rates of: (**a**) 0.01 s^{-1}; (**b**) 0.1 s^{-1}; (**c**) 1 s^{-1}; and (**d**) 10 s^{-1}.

3.3. Constitutive Equation

The corrected peak-stress data were correlated with deformation temperature and strain rate using the Arrhenius-type constitutive framework [25]:

$$\dot{\varepsilon} = A_1 \sigma^{n_1} \exp\left(-\frac{Q}{RT}\right), (\alpha\sigma < 0.8) \tag{10}$$

$$\dot{\varepsilon} = A_2 \exp(\beta\sigma) \exp\left(-\frac{Q}{RT}\right), (\alpha\sigma > 1.2) \tag{11}$$

$$\dot{\varepsilon} = A[\sinh(\alpha\sigma)]^n \exp\left(-\frac{Q}{RT}\right), (\textit{for all stress levels}) \tag{12}$$

where $\dot{\varepsilon}$ is the strain rate (s^{-1}), Q is the hot-deformation activation energy (J mol^{-1}), R is the gas constant (8.314 J mol^{-1} K^{-1}), σ_p is the corrected peak stress (MPa), and T is the absolute temperature (K). $A1$, $A2$, A, $n1$, n, α, and β are material constants. The power-law, exponential, and hyperbolic-sine forms are used for low-, high-, and full-stress ranges, respectively.

Linearization of Equations (10)–(12) gives

$$\ln \dot{\varepsilon} = \ln A_1 + n_1 \ln \sigma - \frac{Q}{RT} \tag{13}$$

$$\ln \dot{\varepsilon} = \ln A_2 + \beta\sigma - \frac{Q}{RT} \tag{14}$$

$$\ln \dot{\varepsilon} = \ln A + n\ln[\sinh(\alpha\sigma)] - \frac{Q}{RT} \tag{15}$$

Equation (15) can be rearranged as

$$\ln [\sinh(\alpha\sigma)] = \frac{Q}{n\mathrm{R}} \cdot \frac{1}{T} + \frac{\ln\left(\frac{\dot{\varepsilon}}{A}\right)}{n} \tag{16}$$

At constant deformation temperature, differentiating Equation (15) with respect to ln[sinh($\alpha\sigma$)] gives

$$n = \left\{ \frac{\partial \ln \dot{\varepsilon}}{\partial \ln[\sinh(\alpha\sigma)]} \right\}_T \tag{17}$$

At constant strain rate, differentiating Equation (16) with respect to $1/T$ gives

$$k = \frac{Q}{n\mathrm{R}} = \left\{ \frac{\partial \ln[\sinh(\alpha\sigma)]}{\partial\left(\frac{1}{T}\right)} \right\}_{\dot{\varepsilon}} \tag{18}$$

The apparent hot-deformation activation energy is therefore calculated as

$$Q = \mathrm{R}nk = \left\{ \frac{\partial \ln \dot{\varepsilon}}{\partial \ln[\sinh(\alpha\sigma)]} \right\}_T \times \left\{ \frac{\partial \ln[\sinh(\alpha\sigma)]}{\partial\left(\frac{1}{T}\right)} \right\} \tag{19}$$

The corrected peak stresses were substituted into the linearized relations. The slopes of the $\ln \dot{\varepsilon} - \ln \sigma_p$ and $\ln \dot{\varepsilon} - \sigma_p$ plots in Figure 4a,b were used to determine n_1 and β, from which $\alpha = \beta/n_1 = 0.0038$ MPa^{-1}. The $\ln \dot{\varepsilon} - \ln[\sinh(\alpha\sigma_p)]$ and $\ln[\sinh(\alpha\sigma_p)] - 1000/T$ plots in Figure 4c,d gave $n = 3.361$ and $Q = 493{,}329.434$ J mol^{-1} ($\approx$493.3 kJ mol^{-1}).

The Zener–Hollomon parameter, Z, was used to combine the effects of temperature and strain rate into a single temperature-compensated strain-rate term [28]:

$$Z = \dot{\varepsilon} \exp\left(\frac{Q}{\mathrm{RT}}\right) = A[\sinh(\alpha\sigma)]^n, \tag{20}$$

Taking the natural logarithm of Equation (20) gives

$$\ln Z = \ln A + n\ln[\sinh(\alpha\sigma)], \tag{21}$$

As shown in Figure 5, ln Z varies linearly with ln[sinh($\alpha\sigma_p$)] with $R^2 = 0.9773$. The fitted intercept gives ln A = 42.9137, corresponding to $A = 1.739 \times 10^{18}$.

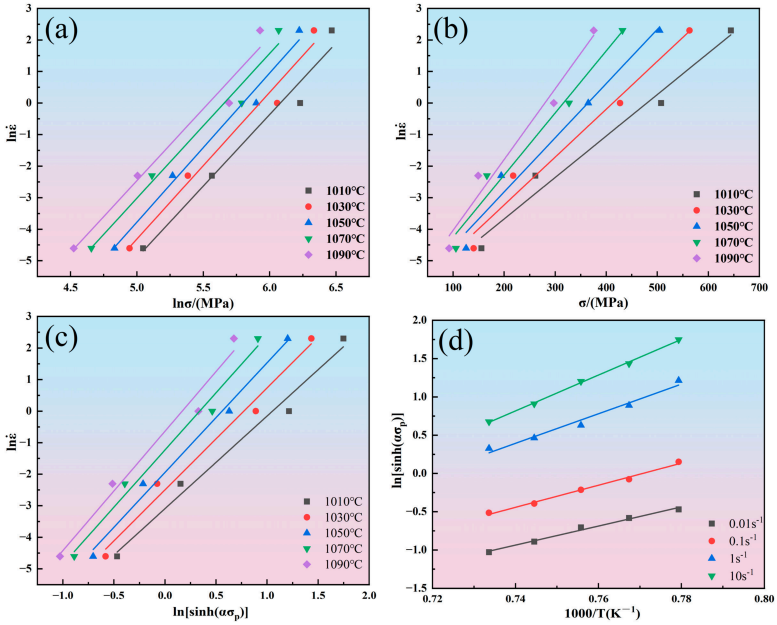

Figure 4. Linear fitting relationships used to determine the constitutive parameters: (**a**) $\ln\dot{\varepsilon} - \ln\sigma_p$; (**b**) $\ln\dot{\varepsilon} - \sigma_p$; (**c**) $ln\dot{\varepsilon} - ln\left[sinh\left(\alpha\sigma_p\right)\right]$; (**d**) $\ln[\sinh(\alpha\sigma_p)] - 1000/T$.

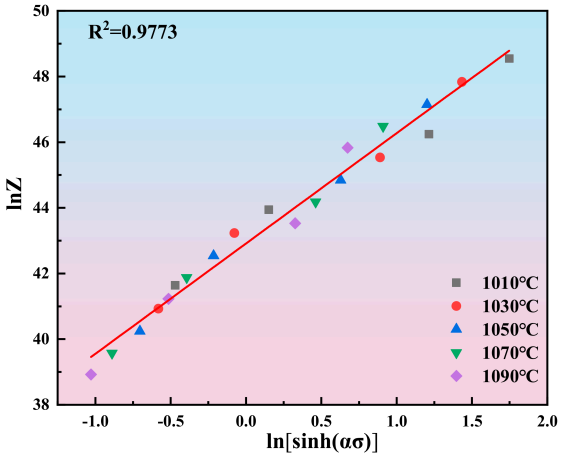

Figure 5. Relationship between peak stress and Z function of GTD222 alloy.

The resulting peak-stress constitutive relation for GTD222 alloy is therefore

$$\dot{\varepsilon} = 1.739 \times 10^{18}[\sinh(0.0038\sigma)]^{3.361}\exp(-\frac{493.3 \times 10^3}{RT}), \quad (22)$$

Peak-stress equations describe only a characteristic point on the flow curve and do not explicitly account for the evolution of stress with accumulated strain [29,30]. Because the apparent constitutive parameters vary with strain during hot deformation [31,32], α, n, Q, and A were recalculated at true strains from 0.1 to 1.2 at intervals of 0.1. Their strain dependences are shown in Figure 6 [33,34]. Following Refs. [35,36], each parameter was fitted by the sixth-order polynomial in Equation (23), with the coefficients listed in Table 3:

$$P = k_0 + k_1\varepsilon + k_2\varepsilon^2 + k_3\varepsilon^3 + k_4\varepsilon^4 + k_5\varepsilon^5 + k_6\varepsilon^6 + \cdots \quad (23)$$

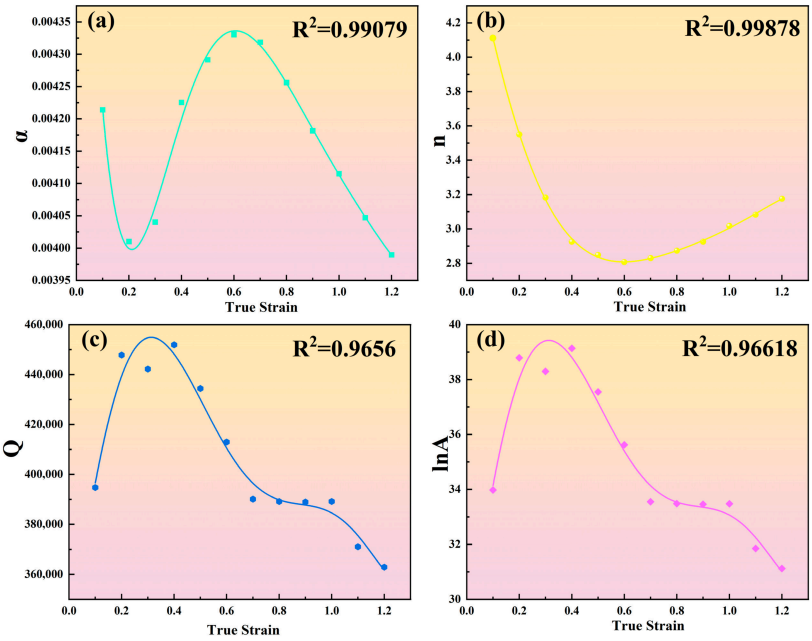

Figure 6. Relationship between material parameters and true strain: (**a**) α-ε; (**b**) n-ε; (**c**) Q-ε; (**d**) LnA-ε.

Table 3. Polynomial fitting results of α, n, lnA, and Q for the GTD222 alloy.

	α	n	Q (J/mol)	lnA
k_0	0.00508	4.83058	3.32×10^5	28.2066
k_1	−0.01363	−7.8229	6.83×10^5	64.00158
k_2	0.0603	4.92207	1.06×10^5	−1.35647
k_3	0.11641	17.105	-6.38×10^6	−552.82262
k_4	0.11293	−33.28795	1.24×10^7	1096.02527
k_5	−0.05478	22.94965	-9.15×10^6	−813.93326
k_6	0.0163	−5.6905	2.38×10^6	212.94472

Substituting the strain-dependent material parameters into the Arrhenius relation gives the strain-compensated constitutive model in Equation (24):

$$\sigma = \frac{1}{\alpha}\ln\left\{\left(\frac{Z}{A}\right)^{\frac{1}{n}} + \left[\left(\frac{Z}{A}\right)^{\frac{2}{n}} + 1\right]^{\frac{1}{2}}\right\} \tag{24}$$

The agreement between the strain-compensated model and the experimental data is shown in Figure 7. The correlation coefficient R and AARE were used to quantitatively evaluate the fitting performance of the model [37], as expressed in Equations (25) and (26):

$$R = \frac{\sum_{i=1}^{S}\left(\sigma_{ei} - \overline{\sigma_e}\right)\left(\sigma_{yi} - \overline{\sigma_y}\right)}{\sqrt{\sum_{i=1}^{S}\left(\sigma_{ei} - \overline{\sigma_e}\right)^2}\sqrt{\sum_{i=1}^{S}\left(\sigma_{yi} - \overline{\sigma_y}\right)^2}} \tag{25}$$

$$AARE = \frac{1}{S}\sum_{i=1}^{S}\left|\frac{\sigma_{ei} - \sigma_{yi}}{\sigma_{ei}}\right| \times 100\% \tag{26}$$

In these equations, S is the total number of paired stress data used for evaluation; σ_{ei} and σ_{yi} represent the corrected experimental flow stress and the corresponding flow stress calculated by the strain-compensated model at the *i*th data point, respectively; and $\bar{\sigma}_e$ and $\bar{\sigma}_y$ are the mean values of the experimental and calculated flow stresses, respectively. The model gives R = 0.978 and AARE = 6.89%, indicating good agreement between the calcu-

lated stresses and the experimental data used for model calibration. However, validation under independent deformation conditions would be required to further assess the external predictive capability of the model.

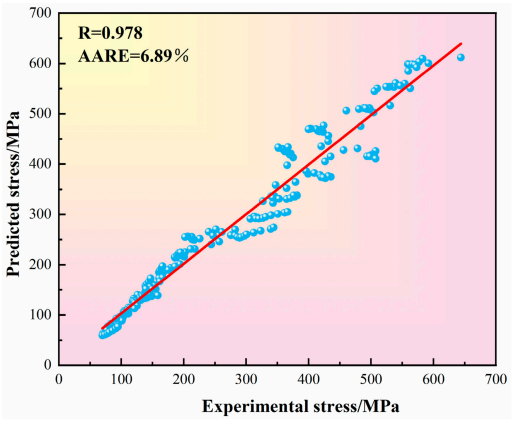

Figure 7. Correlation between calculated values and experimental values.

3.4. Hot Processing Map

The processing map was constructed within the dynamic materials model (DMM) framework [38]. The power input per unit volume, P, is partitioned into the content, G, associated mainly with plastic deformation and heat generation, and the co-content, J, associated with microstructural evolution:

$$P = \sigma\dot{\varepsilon} = G + J = \int_0^{\dot{\varepsilon}} \sigma \mathrm{d}\dot{\varepsilon} + \int_0^{\sigma} \dot{\varepsilon} d\sigma \tag{27}$$

At a fixed deformation temperature, the relationship between flow stress and strain rate is expressed as

$$\sigma = K\varepsilon^m \tag{28}$$

where K is a constant and m is the strain-rate sensitivity. m is obtained from

$$\mathrm{m} = \frac{\partial J}{\partial G} = \frac{\dot{\varepsilon}\partial\sigma}{\sigma\partial\dot{\varepsilon}} = \frac{\partial(\lg\sigma)}{\partial(\lg\dot{\varepsilon})} \tag{29}$$

Combining Equations (28) and (29) gives

$$J = \int_0^{\dot{\varepsilon}} \sigma d\dot{\varepsilon} = \frac{m}{m+1}\sigma\dot{\varepsilon} \tag{30}$$

For an ideal linear dissipater (m = 1), J reaches its maximum value, J_{max}:

$$J_{max} = \frac{\sigma\dot{\varepsilon}}{2} \tag{31}$$

The dimensionless power-dissipation efficiency, η, is defined by normalizing J with respect to J_{max}:

$$\eta = \frac{J}{J_{max}} = \frac{2m}{m+1} \tag{32}$$

Flow instability was evaluated using the Prasad criterion [39]:

$$\xi(\dot{\varepsilon}) = \frac{\partial lg\left(\frac{m+1}{m}\right)}{\partial lg(\dot{\varepsilon})} + m < 0 \tag{33}$$

A negative value of the Prasad instability parameter, ξ, was taken to indicate a predicted flow-instability region. Contours of power-dissipation efficiency were overlaid with the $\xi < 0$ regions to obtain the processing maps. Maps were generated at true strains of 0.3, 0.6, 0.9, and 1.2 so that changes with accumulated deformation could be assessed.

Figure 8 presents the processing maps of the GTD222 alloy at true strains of 0.3, 0.6, 0.9, and 1.2. The predicted instability domains vary with accumulated strain, indicating that the hot-working response cannot be adequately represented by a processing map constructed only at the terminal strain. Nevertheless, the low-strain-rate region around 1070–1090 °C and 0.01–0.1 s^{-1} remains outside the major instability domains over the investigated strain range and exhibits relatively high power-dissipation efficiency. This region is therefore considered a favorable hot-working domain for the GTD222 alloy. Representative microstructures corresponding to different processing conditions are shown in Figure 9. At 1010 °C/1 s^{-1} (Figure 9a), strongly elongated grains and pronounced band-like heterogeneous regions are observed, together with only limited fine DRX grains. Incomplete recrystallization alone is not regarded as direct evidence of flow instability; rather, the instability interpretation is supported by the obvious localized and heterogeneous deformation features observed in the microstructure. When the strain rate is reduced to 0.1 s^{-1} at 1010 °C (Figure 9b), the microstructure becomes substantially more recrystallized and less heterogeneous. At 1050 °C/0.1 s^{-1} (Figure 9c), fine DRX grains are more extensively developed, but locally continuous unrecrystallized or partially recrystallized regions are still retained, indicating that the original deformed structure has not yet been completely replaced by an equiaxed recrystallized microstructure. In contrast, at 1070 °C/0.01 s^{-1} (Figure 9d), these residual deformation features are no longer evident, and the microstructure is dominated by relatively homogeneous equiaxed recrystallized grains. Similar recrystallized morphologies are observed at 1090 °C/0.01 s^{-1} and 1090 °C/0.1 s^{-1} (Figure 9e,f). Together with the strain-dependent processing maps, these microstructural observations provide further support for identifying 1070–1090 °C and 0.01–0.1 s^{-1} as a favorable hot-working domain.

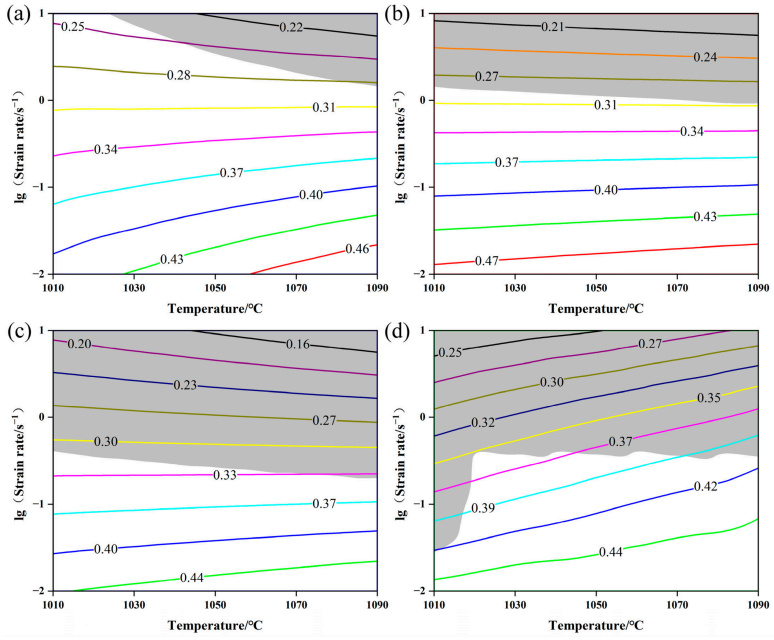

Figure 8. Processing maps of the GTD222 alloy at different true strains: (**a**) 0.3; (**b**) 0.6; (**c**) 0.9; (**d**) 1.2.

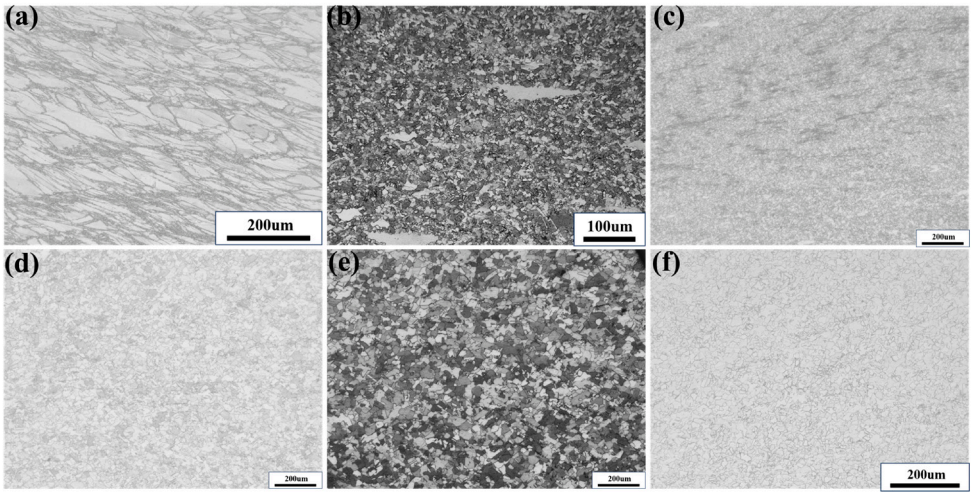

Figure 9. Microstructure corresponding to hot processing map of GTD222 alloy: (**a**) 1010 °C-1 s^{-1}, (**b**) 1010 °C-0.1 s^{-1}, (**c**) 1050 °C-0.1 s^{-1}, (**d**) 1070 °C-0.01 s^{-1}, (**e**) 1090 °C-0.01 s^{-1}, (**f**) 1090 °C-0.1 s^{-1}.

3.5. Microstructure Evolution

3.5.1. Effect of Deformation Temperature on Microstructure

Dynamic recrystallization during hot deformation is governed by the evolution of dislocations and the migration of grain boundaries. Dislocation storage raises the internal energy of the deformed matrix and provides a driving force for recrystallization, whereas the subsequent removal of deformation substructure and the growth of newly formed grains depend strongly on boundary mobility [5]. Because both dislocation processes and grain-boundary migration are temperature sensitive, the deformation temperature has a direct influence on the recrystallization response of GTD222. At 1010 °C (Figure 10(a1)), elongated grains and residual deformed regions are still present, indicating that the transformation to a recrystallized structure is not complete. The lower temperature limits dislocation mobility, recovery, and grain-boundary migration, thereby reducing the rate at which the retained deformation structure is consumed. According to the GOS analysis in Figure 10(a3–c3), the DRX fractions at 1010, 1050, and 1090 °C are 80.29%, 79.09%, and 81.96%, respectively. These values show no monotonic dependence on temperature: the DRX fraction decreases slightly from 1010 to 1050 °C and then rises again at 1090 °C. Since the differences among the three values are relatively small, the temperature appears to exert only a modest influence on the final DRX fraction over the investigated range. A clearer temperature effect is observed in the morphology of the recrystallized structure. As the temperature increases, enhanced dislocation mobility, recovery, and grain-boundary migration facilitate the elimination of deformation substructure and promote further growth of recrystallized grains. Consequently, the microstructure becomes more homogeneous, and the recrystallized grains become coarser. Thus, within the present temperature interval, increasing the temperature affects the development and growth of the recrystallized microstructure more strongly than it affects the overall DRX fraction.

The grain-size data in Figure 11 confirm this trend. At 0.1 s^{-1}, recrystallized grains become progressively larger as the deformation temperature increases. Enhanced boundary mobility at higher temperature facilitates both the completion of recrystallization and subsequent growth of the recrystallized grains [40], so the final structure becomes coarser even though the DRX fraction changes only slightly.

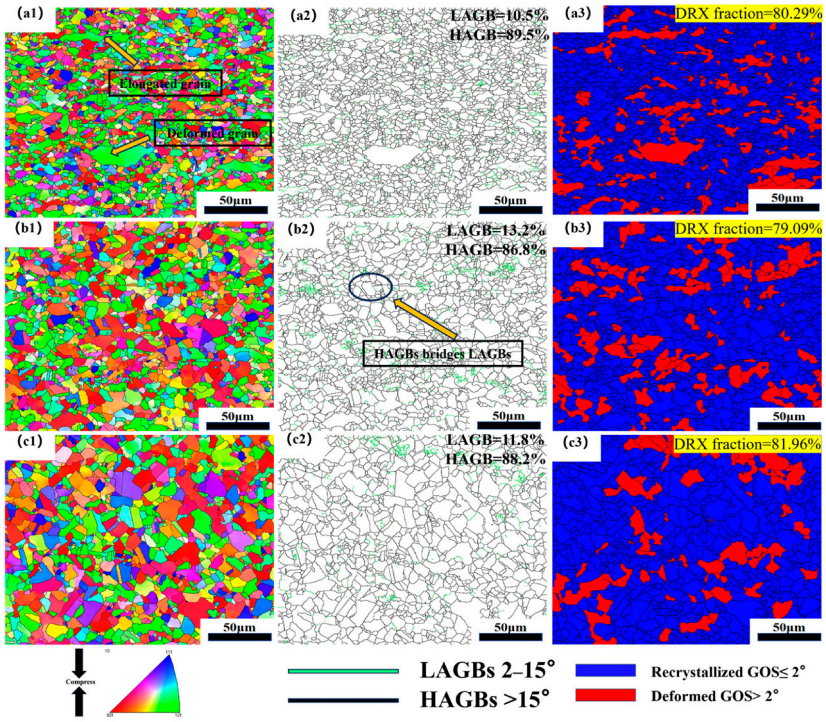

Figure 10. Effect of different temperatures on microstructure of GTD222 alloy at 0.1 s^{-1}: (**a1**–**a3**) 1010 °C; (**b1**–**b3**) 1050 °C; (**c1**–**c3**) 1090 °C; (**a1**), (**b1**), (**c1**) IPF maps; (**a2**), (**b2**), (**c2**) GB maps; (**a3**), (**b3**), (**c3**) GOS maps.

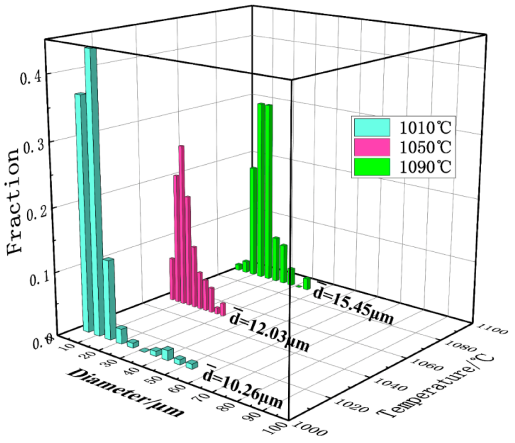

Figure 11. The grain size of GTD222 alloy at different temperatures at 0.1 s^{-1}.

3.5.2. Effect of Strain Rate on Microstructure

Figure 12 shows the effect of strain rate on the microstructural evolution of the GTD222 alloy deformed at 1090 °C. At 0.01 s^{-1}, the relatively long deformation time provides sufficient opportunity for thermally activated diffusion and grain-boundary migration, thereby promoting extensive recrystallization and the subsequent growth of recrystallized grains. Consequently, the microstructure exhibits a high DRX fraction of 84.51% together with relatively coarse recrystallized grains [41,42]. Pronounced grain-boundary bulging is also observed in Figure 12(a1). Such boundary morphology is closely associated with strain-induced boundary migration (SIBM), which is an important feature of DDRX [43]. In addition, several fine recrystallized grains can be observed within the coarse recrystallized regions, indicating that further recrystallization-related structural evolution may occur locally during continued deformation. When the strain rate increases to 1 s^{-1}, the microstructure changes markedly, as shown in Figure 12(c1–c3). A large fraction of the

original grains remains strongly elongated along the deformation direction, whereas fine equiaxed recrystallized grains are distributed along the prior HAGBs and form a typical necklace-like structure. These morphological features are characteristic of DDRX [42]. The DRX fraction decreases to 46.13%, while the LAGB fraction increases to 29.4%, indicating that a considerable amount of deformation substructure remains in the final microstructure. The reduced deformation time at this strain rate limits grain-boundary migration as well as the development and growth of newly recrystallized grains, resulting in incomplete recrystallization. As indicated by the circled regions in Figure 12(c1–c3), a small number of fine intragranular grains enclosed by HAGBs are also present within the retained deformed grains. Their intragranular location, together with the orientation-gradient and misorientation evidence discussed subsequently, is consistent with progressive subgrain rotation and boundary-misorientation accumulation associated with CDRX [16]. Therefore, CDRX is considered to make a supplementary contribution to the overall recrystallization process, although the final-state microstructure alone cannot directly demonstrate the complete progressive transformation from LAGBs to HAGBs.

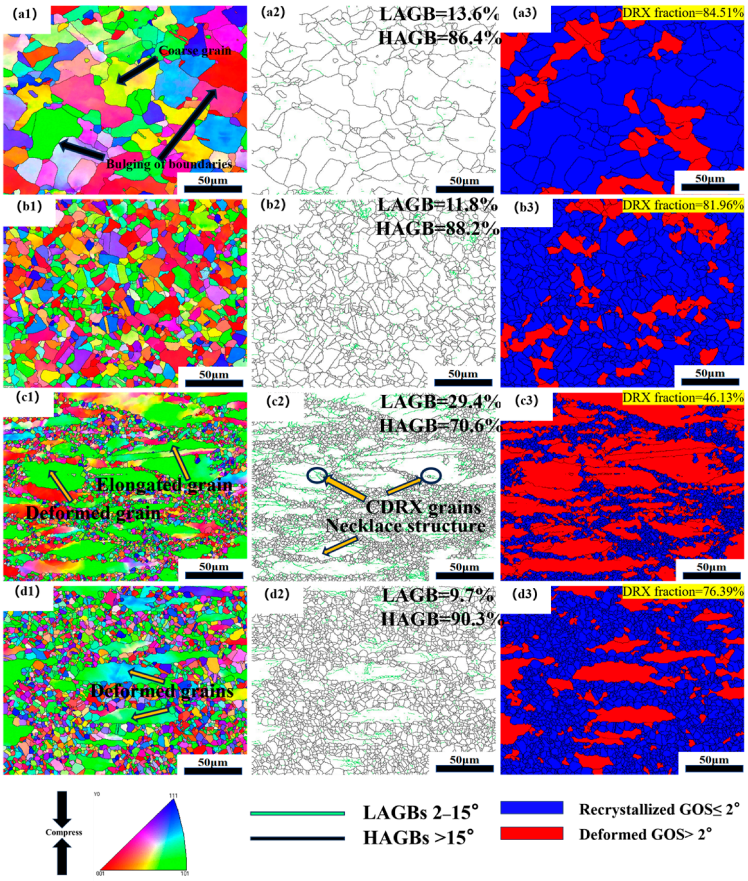

Figure 12. Effect of different strain rates on microstructure of GTD222 alloy at 1090 °C: (**a1–a3**) 0.01 s^{-1}; (**b1–b3**) 0.1 s^{-1}; (**c1–c3**) 1 s^{-1}; (**d1–d3**) 10 s^{-1}; (**a1**), (**b1**), (**c1**), (**d1**) IPF maps; (**a2**), (**b2**), (**c2**), (**d2**) GB maps; (**a3**), (**b3**), (**c3**), (**d3**) GOS maps.

The effect of strain rate on DRX is not strictly monotonic. At 10 s^{-1}, large retained deformed regions and necklace-like recrystallized structures are still observed in Figure 12(d1–d3); however, the DRX fraction increases again to 76.39%, and the HAGB fraction rises to 90.3%, both higher than those obtained at 1 s^{-1}. This increase may be related to the combined effects of increased deformation storage energy and stronger deformation heating at the highest strain rate. Rapid dislocation accumulation can increase the driving force for recrystallization, while deformation-induced temperature rise may

enhance thermally activated dislocation motion and grain-boundary migration, partly compensating for the reduced deformation time. Therefore, the final microstructure reflects the competition among deformation time, stored deformation energy, and deformation heating rather than a simple monotonic dependence of DRX on strain rate.

4. Discussion

The extent of DRX and the associated grain-size evolution are closely related to the underlying recrystallization mechanisms. Therefore, the DRX mechanisms governing the microstructural evolution of the GTD222 alloy during hot deformation require further analysis [44]. The development of DRX is closely associated with local lattice distortion and dislocation accumulation. Kernel average misorientation (KAM) was therefore used to qualitatively evaluate local misorientation gradients associated with plastic deformation [45,46]. In the KAM analysis, a maximum neighboring-misorientation threshold of 5° was adopted. The corresponding KAM maps obtained after isothermal compression under different deformation conditions are presented in Figure 13.

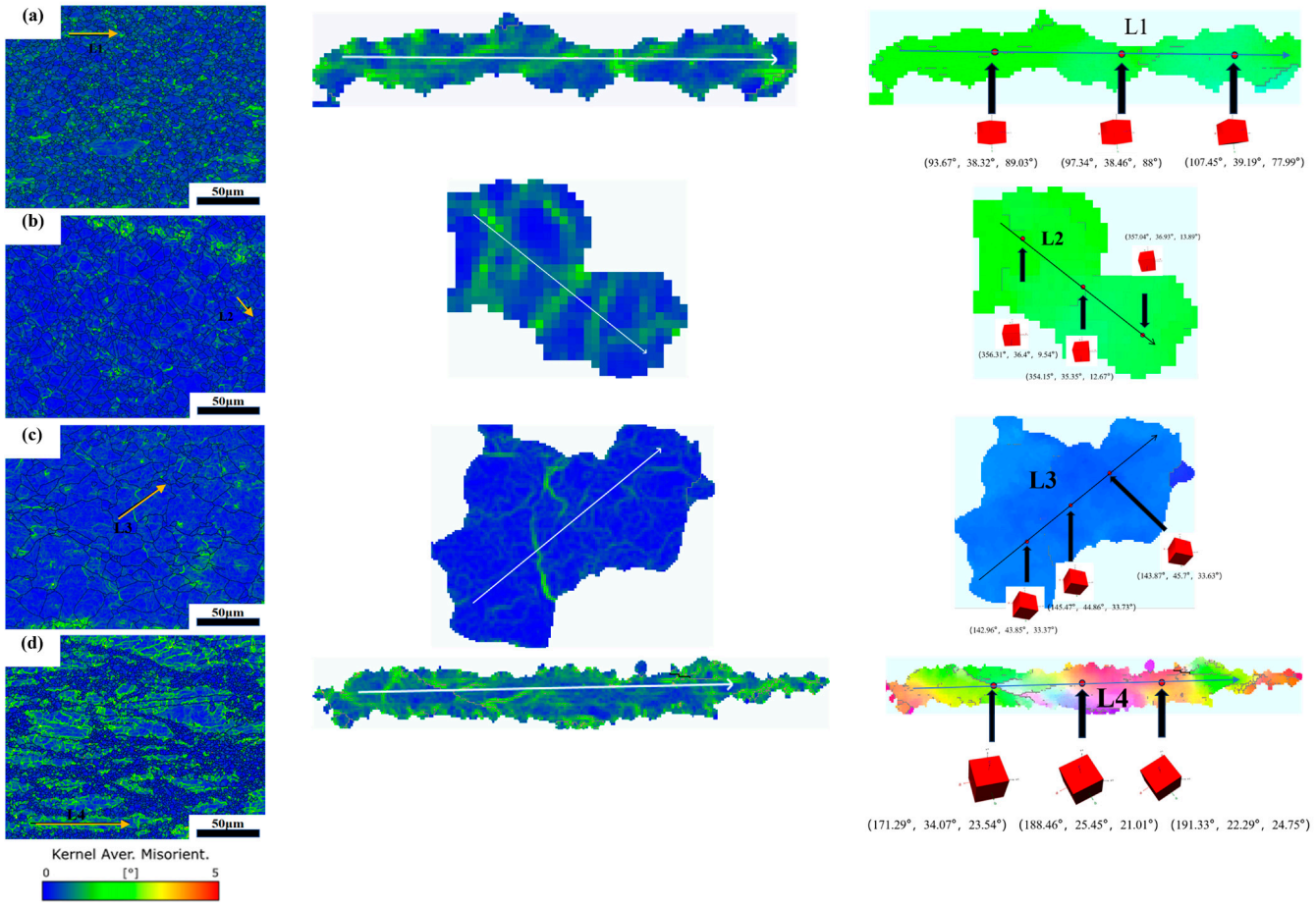

Figure 13. KAM maps (left), high magnification (mid), and IPF map (right) of the samples during hot deformation: (**a**) 1010 °C–0.1 s^{-1}; (**b**) 1090 °C–0.1 s^{-1}; (**c**) 1090 °C–0.01 s^{-1}; (**d**) 1090 °C–1 s^{-1}.

4.1. DDRX Mechanism

As shown in Figure 13a, the relatively low deformation temperature of 1010 °C limits grain-boundary mobility. Under this condition, DDRX-related nucleation is mainly associated with the initial bulging of grain boundaries through SIBM [43]. Local differences in stored deformation energy caused by heterogeneous dislocation accumulation provide the driving force for boundary bulging toward regions of higher dislocation density. However,

the limited thermal activation at 1010 °C restricts grain-boundary migration, so only limited bulging and incomplete recrystallization are observed in the retained deformed regions. When the temperature increases to 1090 °C, grain-boundary mobility is enhanced, and the SIBM process becomes more pronounced. Grain-boundary bulging develops more extensively, facilitating the formation and growth of recrystallized grains along prior grain boundaries. At the same time, intragranular orientation gradients and subgrain-related misorientation are also observed. These intragranular features are consistent with progressive subgrain rotation and therefore suggest a supplementary contribution from CDRX rather than an additional DDRX nucleation route. Thus, the final microstructure at 1090 °C reflects the combined action of dominant DDRX and supplementary CDRX-related evolution. When the strain rate decreases to 0.01 s^{-1}, the overall recrystallized morphology remains similar to that at 0.1 s^{-1}, but the recrystallized grains become noticeably coarser. The lower strain rate provides more time for grain-boundary migration and the growth of recrystallized grains at 1090 °C. As deformation proceeds, bulged boundaries can migrate into the deformed matrix, progressively consuming the retained deformed regions and promoting grain growth. This behavior is consistent with the later-stage growth characteristics associated with DDRX. The driving force for such boundary migration is related to the stored-energy difference across the boundary, while the longer deformation time at low strain rate allows more extensive migration and grain growth. In contrast, when the strain rate increases to 1 s^{-1} (Figure 13d), the deformation time becomes much shorter, restricting grain-boundary migration and the growth of newly recrystallized grains. Fine recrystallized grains therefore develop mainly along prior grain boundaries and form a continuous necklace-like structure, while a considerable fraction of elongated deformed grains is retained. The shorter deformation time also limits the dislocation rearrangement and dynamic recovery within the deformed matrix, resulting in stronger intragranular orientation gradients and a higher fraction of retained deformation substructure. Under this condition, DDRX is characterized by grain-boundary bulging and necklace-like recrystallization, but its growth is incomplete because of the limited time available for boundary migration. Overall, the results indicate that the grain-boundary mobility is strongly affected by the deformation temperature and strain rate. Higher temperature and lower strain rate generally provide more favorable conditions for grain-boundary migration and the growth of DDRX grains, whereas higher strain rates promote greater retention of deformed substructure. The observed intragranular orientation gradients further suggest that CDRX makes a supplementary contribution under selected conditions.

TEM provides additional morphological evidence for this interpretation. After deformation at 1010 °C/0.1 s^{-1} (Figure 14a), pronounced grain-boundary bulging and a triple-junction configuration are visible, both of which are commonly associated with DDRX nucleation. At 1090 °C/0.1 s^{-1} (Figure 14b,c), boundary bulging remains evident and serrated boundaries are also observed. Similar bulging and serration occur at 1090 °C/1 s^{-1} (Figure 14d–f). Regions adjacent to the serrated boundaries contain a high density of dislocations; local differences in stored deformation energy can promote irregular boundary migration and help generate such serrated morphologies [47]. Twin-related features are also present. Those within recrystallized grains are consistent with annealing twins, whereas features associated with strongly deformed regions may be related to deformation twinning. Overall, the TEM observations support DDRX-related grain-boundary evolution over the investigated strain-rate range without requiring the mechanism to be inferred from flow-curve shape alone.

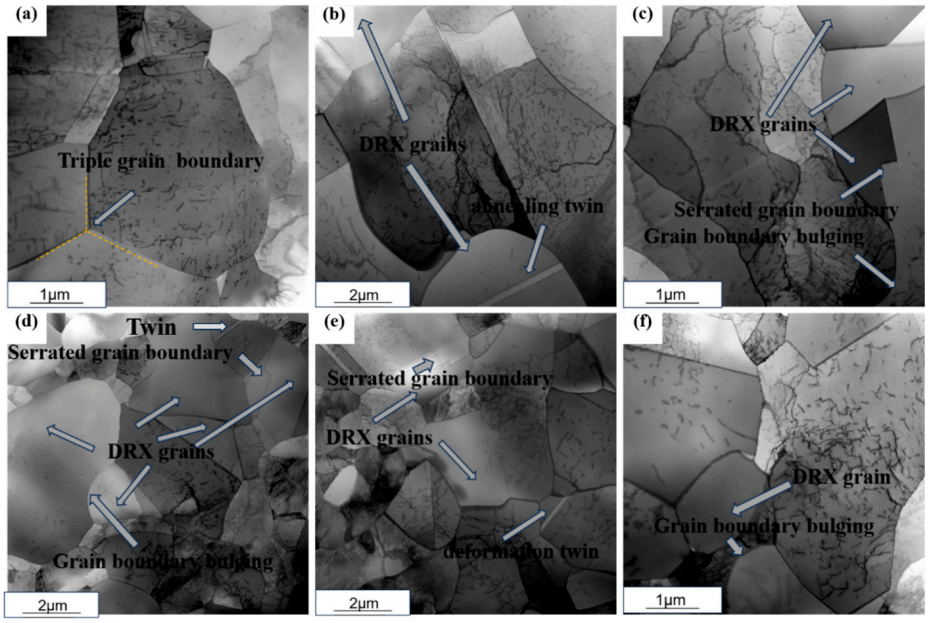

Figure 14. TEM Image of GTD222 alloy after hot deformation: (**a**) 1010 °C–0.1 s^{-1}; (**b**,**c**) 1090 °C–0.1 s^{-1}; (**d**–**f**) 1090 °C –1 s^{-1}.

4.2. CDRX Mechanism

CDRX is generally regarded as a progressive microstructural evolution process [48]. During CDRX, dislocation rearrangement promotes the formation of partially or fully enclosed subgrains bounded mainly by LAGBs. With continued straining, progressive subgrain rotation increases the misorientation across these boundaries. Consequently, some LAGBs may gradually evolve toward medium- and high-angle grain boundaries, eventually giving rise to newly recrystallized grains enclosed by HAGBs [49]. Therefore, intragranular orientation gradients and the evolution of boundary misorientation can provide useful evidence for assessing a possible contribution from CDRX [42].

The line scans selected from the KAM maps in Figure 13 were used to examine orientation changes within the retained deformed grains. Crystallographic orientations at three representative positions on each line are shown by orientation cubes together with the corresponding Euler angles. The intragranular orientation changes reveal pronounced orientation subdivision and are consistent with subgrain-related lattice rotation. At 0.1 s^{-1}, the retained orientation gradient is weaker after deformation at 1090 °C than at 1010 °C (Figure 13a,b), which is consistent with more effective recovery, recrystallization, and grain-boundary migration at the higher temperature. In contrast, increasing the strain rate from 0.1 to 1 s^{-1} at 1090 °C (Figure 13b,d) leaves a stronger orientation gradient because less time is available to remove the deformation substructure. The misorientation profiles in Figure 15 quantify these differences. At 1090 °C/1 s^{-1}, the point-to-origin misorientation reaches approximately 26.73° over 23.44 μm and is accompanied by appreciable local point-to-point changes. At 1090 °C/0.1 s^{-1}, the cumulative value is only 6.51° over 9.34 μm, whereas at 1010 °C/0.1 s^{-1} it exceeds 12.16° over the same distance. These orientation gradients, together with the fine intragranular grain showing CDRX-related characteristics in Figure 12(c2), indicate that CDRX-related features are more pronounced at 1 s^{-1} than at 0.1 s^{-1} under the present conditions. The KAM maps and misorientation profiles therefore support a contribution from CDRX to the final microstructure. They do not, however, directly record the strain-resolved transformation of LAGBs into HAGBs; that progressive sequence remains a mechanistic interpretation because interrupted-deformation experiments were not performed.

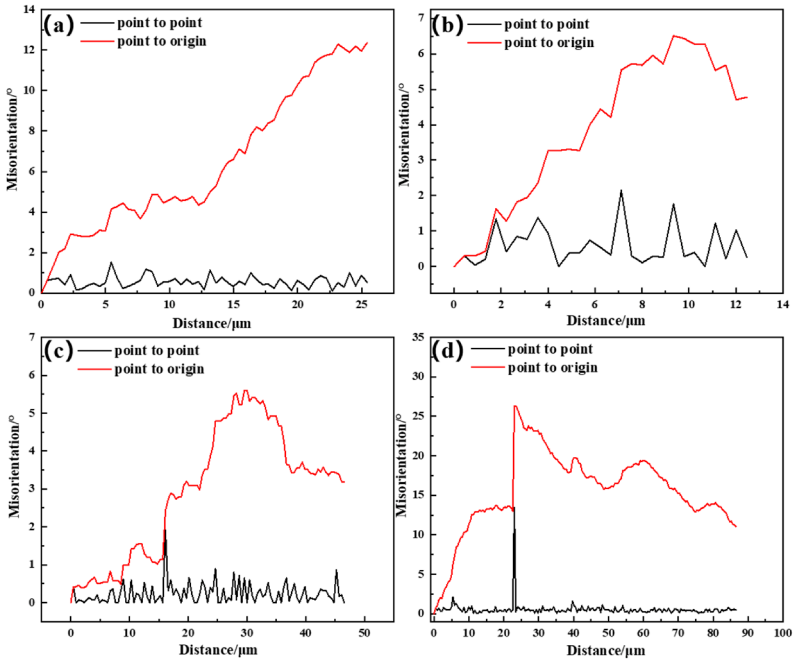

Figure 15. Misorientation profiles along the lines indicated in Figure 13: (**a**) L1; (**b**) L2; (**c**) L3; and (**d**) L4.

For the CDRX analysis, the 10–15° portion of the LAGB population was additionally designated as medium-angle grain boundaries (MAGBs), following Refs. [46,50,51]. MAGBs are therefore a subrange of LAGBs in this work, not a separate mutually exclusive boundary class. Figure 16 shows that their retained fraction depends strongly on deformation condition and reaches its highest value at 1090 °C/1 s^{-1}. The larger fraction at this condition is consistent with stronger retention of intragranular subdivision and intermediate boundary misorientation when deformation is rapid. At lower rates, the longer available time favors recovery, boundary migration, and recrystallized-grain growth, which can reduce the number of intermediate-misorientation boundaries retained in the final structure. Together with the KAM and line-profile results, the MAGB data provide additional support for a CDRX contribution. Figure 17 schematically summarizes the proposed DDRX and CDRX pathways.

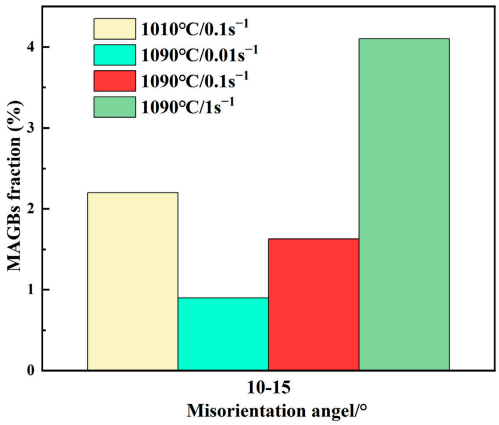

Figure 16. Variation in the fraction of medium-angle grain boundaries (MAGBs) during hot deformation under different deformation conditions.

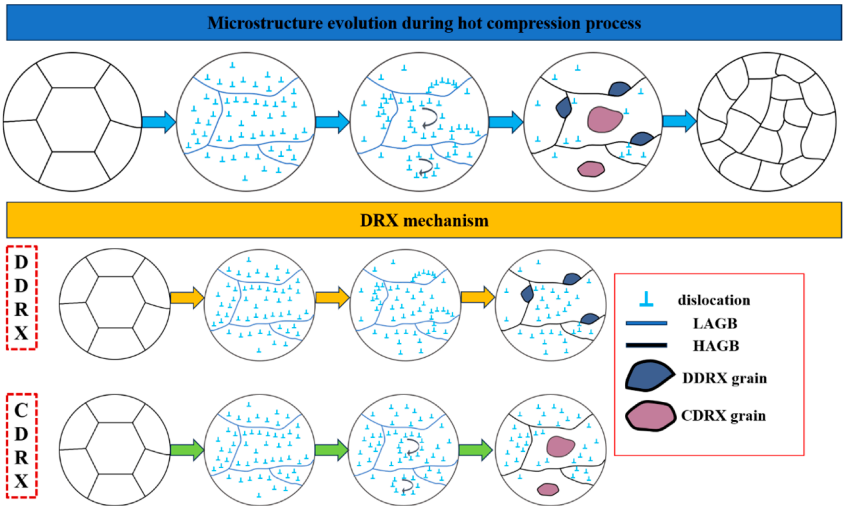

Figure 17. Microstructure evolution and DRX mechanism diagram of GTD222 alloy during hot deformation process.

5. Conclusions

The hot-deformation response and microstructural evolution of GTD222 were examined by isothermal compression over the investigated temperature and strain-rate ranges. The principal findings are summarized as follows:

(1) The corrected flow resistance decreases as the deformation temperature increases or the strain rate decreases. After accounting for interfacial friction and adiabatic heating, a strain-compensated Arrhenius-type constitutive model was established. For the dataset used to calibrate the model, R = 0.978 and AARE = 6.89%, indicating close agreement between calculated and experimental stresses.

(2) Strain-dependent processing maps at ε = 0.3, 0.6, 0.9, and 1.2, interpreted together with the corresponding microstructures, support 1070–1090 °C and 0.01–0.1 s^{-1} as a favorable hot-working domain. Conditions examined within this region show predominantly equiaxed and comparatively homogeneous recrystallized structures.

(3) The recrystallized structure is sensitive to both temperature and strain rate, but the DRX fraction is not monotonic with either variable. At 0.1 s^{-1}, increasing temperature is expressed more clearly through recrystallized-grain growth than through a systematic change in DRX fraction. At 1090 °C, the DRX fraction decreases to 46.13% at 1 s^{-1} and then rises to 76.39% at 10 s^{-1}, a response that may reflect the combined influence of stored deformation energy and deformation heating.

(4) The dominant recrystallization mode is DDRX, as indicated by grain-boundary bulging, serrated boundaries, and necklace-like distributions of fine recrystallized grains. CDRX also contributes: intragranular orientation gradients, cumulative misorientation, subgrain-related orientation subdivision, MAGB development, and fine intragranular grains are all consistent with this supplementary mechanism. Because the evidence is obtained from final-state microstructures, the progressive LAGB-to-HAGB sequence associated with CDRX is inferred rather than directly observed.

Author Contributions: Z.Z.: Investigation, Methodology, Data curation, Formal analysis, Visualization, Writing–original draft. C.X.: Resources, Investigation, Validation. G.W.: Resources, Investigation, Validation. C.M.: Resources, Methodology, Validation. M.W.: Conceptualization, Project administration, Funding acquisition, Supervision, Writing—review and editing. M.L.: Conceptualization, Supervision, Project administration, Writing—review and editing. All authors have read and agreed to the published version of the manuscript.

Funding: This research was funded by the Science and Technology Program of Guizhou Province (Grant No. (2026) 198, the National Science and Technology Major Project (Nos. 2024ZDO713601-11), the Guizhou Province Basic Research Program Youth Guidance Project (QKHJC QN (2025) 451).

Data Availability Statement: The original contributions presented in this study are included in the article material. Further inquiries can be directed to the corresponding author.

Acknowledgments: This work was supported by the Science and Technology Program of Guizhou Province (Grant No. (2026) 198), the National Science and Technology Major Project (Nos. 2024ZDO713601-11), the Guizhou Province Basic Research Program Youth Guidance Project (QKHJC QN (2025) 451).

Conflicts of Interest: Chunhua Xiang, Guangyu Wang, and Cunqiang Ma are employees of Guizhou Aviation Technical Development Co., Ltd. All authors declare that the research was conducted in the absence of any commercial or financial relationships that could be construed as a potential conflict of interest.

References

1. Wang, L.; Wang, N.; Yao, W.J.; Zheng, Y.P. Effect of substrate orientation on the columnar-to-equiaxed transition in laser surface remelted single crystal superalloys. *Acta Mater.* **2015**, *88*, 283–292. [CrossRef]
2. Yang, H.H.; Yang, J.J.; Huang, W.P.; Wang, Z.M.; Zeng, X.Y. The printability, microstructure, crystallographic features and microhardness of selective laser melted Inconel 718 thin wall. *Mater. Des.* **2018**, *156*, 407–418. [CrossRef]
3. Zhang, Z.; Wang, R.; Lv, Y.; Liu, W.; Liu, Y. Microstructures and mechanical properties of heat treated TiC/GTD222 nickel-based composite prepared by selective laser melting. *Mater. Sci. Eng. A* **2022**, *851*, 143588. [CrossRef]
4. Wen, H.; Tang, X.; Jin, J.; Cai, C.; Yang, H.; Teng, Q.; Wei, Q.; Wang, X.; Zheng, C.; He, Y.; et al. Effect of extrusion ratios on microstructure evolution and strengthening mechanisms of a novel P/M nickel-based superalloy. *Mater. Sci. Eng. A* **2022**, *847*, 143356. [CrossRef]
5. Zhang, H.B.; Zhang, K.F.; Lu, Z.; Zhao, C.H.; Yang, X.L. Hot deformation behavior and processing map of a γ'-hardened nickel-based superalloy. *Mater. Sci. Eng. A-Struct. Mater. Prop. Microstruct. Process.* **2014**, *604*, 1–8. [CrossRef]
6. Chen, X.M.; Lin, Y.C.; Wen, D.X.; Zhang, J.L.; He, M. Dynamic recrystallization behavior of a typical nickel-based superalloy during hot deformation. *Mater. Des.* **2014**, *57*, 568–577. [CrossRef]
7. Lin, Y.C.; Chen, X.M. A critical review of experimental results and constitutive descriptions for metals and alloys in hot working. *Mater. Des.* **2011**, *32*, 1733–1759. [CrossRef]
8. Tan, Y.B.; Ma, Y.H.; Zhao, F. Hot deformation behavior and constitutive modeling of fine grained Inconel 718 superalloy. *J. Alloys Compd.* **2018**, *741*, 85–96. [CrossRef]
9. Song, X.; Tang, Z.; He, X.; Jia, L.; Li, G.; He, J.; Wang, X. Hot deformation behavior and microstructure evolution of a novel as-forged Ni-based superalloy. *J. Alloys Compd.* **2025**, *1024*, 180195. [CrossRef]
10. Liu, D.; Lai, X.; Huang, Z.; Yang, L.; Zhou, K. Study on Hot Deformation Behavior and Processing Maps of Cobalt-Based Superalloy GH5188. *Adv. Eng. Mater.* **2024**, *26*, 2301607. [CrossRef]
11. Liu, L.; Zhao, G.; Wang, G.; Ma, X.; Yan, Z.; Cao, S. Hot deformation behavior and microstructure evolution model of 7055 aluminum alloy. *J. Mater. Res. Technol.* **2023**, *27*, 3191–3213. [CrossRef]
12. Huang, M.; Zhou, Z.; Cui, C.; Wang, X.; Zhang, R.; Tao, X.; Ye, X.-X.; Zhou, Y.; Sun, X. Effect of pre-deformation homogenization on high-temperature deformation behavior and microstructure evolution of a new Ni-W-Cr superalloy. *Mater. Sci. Eng. A* **2025**, *929*, 148112. [CrossRef]
13. Zhong, M.; Yu, H.; Wang, Z.; Zhang, X.; Qu, J. Hot deformation behavior and process parameters optimization of GH4738 nickel-based superalloy. *J. Mater. Res. Technol.* **2024**, *33*, 7990–8001. [CrossRef]
14. Liu, W.; Liu, Z.; Zhang, H.; Ruan, J.; Huang, H.; Zhou, X.; Meng, F.; Zhang, S.; Jiang, L. Hot deformation behavior and new grain size model of hot extruded FGH4096 superalloy during hot compression. *J. Alloys Compd.* **2023**, *938*, 168574. [CrossRef]
15. Li, Y.; Zhang, Y.; Chen, Z.; Ji, Z.; Zhu, H.; Sun, C.; Dong, W.; Li, X.; Sun, Y.; Yao, S. Hot deformation behavior and dynamic recrystallization of GH690 nickel-based superalloy. *J. Alloys Compd.* **2020**, *847*, 156507. [CrossRef]
16. Gao, S.; He, X.K.; Tang, Z.X.; Dong, W.J.; Liu, Z.D.; Bao, H.S. Hot deformation behavior and hot working window of a solid solution strengthened Ni-Cr-Fe-based superalloy. *J. Mater. Res. Technol.* **2024**, *29*, 1377–1389. [CrossRef]
17. Lin, Y.C.; Chen, X.M.; Wen, D.X.; Chen, M.S. A physically-based constitutive model for a typical nickel-based superalloy. *Comput. Mater. Sci.* **2014**, *83*, 282–289. [CrossRef]
18. Jiao, Y.X.; Qi, Q.Q.; Gong, Y.M.; Gao, Y.F.; Chen, H.Q.; Chen, F.; Zhou, F.W.; Li, X.X. Research on hot deformation behavior and microstructure evolution mechanism of GH4169 superalloy. *Mater. Today Commun.* **2024**, *40*, 10. [CrossRef]

19. Kareem, S.A.; Anaele, J.U.; Aikulola, E.O.; Olanrewaju, O.F.; Omiyale, B.O.; Bodunrin, M.O.; Alaneme, K.K. Hot deformation behaviour, constitutive model description, and processing map analysis of superalloys: An overview of nascent developments. *J. Mater. Res. Technol.* **2023**, *26*, 8624–8669. [CrossRef]
20. Jia, D.; Sun, W.; Xu, D.; Yu, L.; Xin, X.; Zhang, W.; Qi, F. Abnormal dynamic recrystallization behavior of a nickel based superalloy during hot deformation. *J. Alloys Compd.* **2019**, *787*, 196–205. [CrossRef]
21. Ebrahimi, R.; Najafizadeh, A. A new method for evaluation of friction in bulk metal forming. *J. Mater. Process. Technol.* **2004**, *152*, 136–143. [CrossRef]
22. Goetz, R.L.; Semiatin, S.L. The adiabatic correction factor for deformation heating during the uniaxial compression test. *J. Mater. Eng. Perform.* **2001**, *10*, 710–717. [CrossRef]
23. Mataya, M.C.; Sackschewsky, V.E. Effect of internal heating during hot compression on the stress-strain behavior of alloy 304L. *Metall. Mater. Trans. A* **1994**, *25*, 2737–2752. [CrossRef]
24. Devadas, C.; Samarasekera, I.V.; Hawbolt, E.B. The thermal and metallurgical state of steel strip during hot rolling: Part III. *Microstruct. Evol. Metall. Trans. A* **1991**, *22*, 335–349. [CrossRef]
25. Sellars, C.M.; McTegart, W.J. On the mechanism of hot deformation. *Acta Metall.* **1966**, *14*, 1136–1138. [CrossRef]
26. Tian, Y.; Zhang, P.; Zhao, G.; Li, H.; Ma, L.; Li, J. A systematic study on thermo-mechanical behavior, processing maps and recrystallization mechanism of Incoloy825 superalloy during hot compression. *J. Mater. Res. Technol.* **2024**, *28*, 4551–4566. [CrossRef]
27. Jia, Z.; Gao, Z.-X.; Ji, J.-J.; Liu, D.-X.; Guo, T.-B.; Ding, Y.-T. High-temperature deformation behavior and processing map of the as-cast Inconel 625 alloy. *Rare Met.* **2021**, *40*, 2083–2091. [CrossRef]
28. Medina, S.F.; Hernandez, C.A. General expression of the Zener-Hollomon parameter as a function of the chemical composition of low alloy and microalloyed steels. *Acta Mater.* **1996**, *44*, 137–148. [CrossRef]
29. Ji, G.L.; Li, F.G.; Li, Q.H.; Li, H.Q.; Li, Z. A comparative study on Arrhenius-type constitutive model and artificial neural network model to predict high-temperature deformation behaviour in Aermet100 steel. *Mater. Sci. Eng. A-Struct. Mater. Prop. Microstruct. Process.* **2011**, *528*, 4774–4782. [CrossRef]
30. Sun, C.Y.; Liu, J.R.; Li, R.; Zhang, Q.D.; Dong, J.X. Constitutive relationship of IN690 superalloy by using uniaxial compression tests. *Rare Met.* **2011**, *30*, 81–86. [CrossRef]
31. Cai, Z.W.; Chen, F.X.; Guo, J.Q. Constitutive model for elevated temperature flow stress of AZ41M magnesium alloy considering the compensation of strain. *J. Alloys Compd.* **2015**, *648*, 215–222. [CrossRef]
32. Wang, Y.J.; Peng, J.; Zhong, L.P.; Pan, F.S. Modeling and application of constitutive model considering the compensation of strain during hot deformation. *J. Alloys Compd.* **2016**, *681*, 455–470. [CrossRef]
33. Wang, K.; Liu, X.; Guo, Y.; Sugio, K.; Sasaki, G. Coupled behavior of dynamic restoration mechanisms and α phase evolution in TC18 titanium alloy during hot deformation. *J. Alloys Compd.* **2025**, *1048*, 185322. [CrossRef]
34. Chen, W.; Ou, M.; Liu, R.; Zhao, Y.; Li, C. Investigation on the high-temperature deformation behavior and recrystallization mechanism of TC18 titanium alloy. *J. Alloys Compd.* **2026**, *1057*, 186904. [CrossRef]
35. Li, C.; Huang, L.; Zhao, M.; Guo, S.; Li, J. Hot deformation behavior and mechanism of a new metastable β titanium alloy Ti–6Cr–5Mo–5V–4Al in single phase region. *Mater. Sci. Eng. A* **2021**, *814*, 141231. [CrossRef]
36. Dong, E.; Yu, W.; Cai, Q.; Cheng, L.; Ning, Z.; Shi, J. High-temperature deformation behavior of TiNi-Nb hypoeutectic alloy. *Mater. Sci. Eng. A* **2019**, *764*, 138228. [CrossRef]
37. Zhao, J.W.; Ding, H.; Zhao, W.J.; Huang, M.L.; Wei, D.B.; Jiang, Z.Y. Modelling of the hot deformation behaviour of a titanium alloy using constitutive equations and artificial neural network. *Comput. Mater. Sci.* **2014**, *92*, 47–56. [CrossRef]
38. Prasad, Y.V.R.K.; Gegel, H.L.; Doraivelu, S.M.; Malas, J.C.; Morgan, J.T.; Lark, K.A.; Barker, D.R. Modeling of dynamic material behavior in hot deformation: Forging of Ti-6242. *Metall. Trans. A* **1984**, *15*, 1883–1892. [CrossRef]
39. Prasad, Y.V.R.K.; Seshacharyulu, T. Modelling of hot deformation for microstructural control. *Int. Mater. Rev.* **1998**, *43*, 243–258. [CrossRef]
40. Zhang, S.Y.; Wang, J.Z.; Huang, L.; Srivatsa, S.; Zhou, K.C.; Huang, Z.W.; Jiang, L. Correction of flow stress data due to non-homogeneous deformation and thermal conditions during hot compression testing of a polycrystalline nickel-base superalloy. *J. Mater. Sci.* **2021**, *56*, 7727–7739. [CrossRef]
41. Zhang, H.B.; Zhang, K.F.; Zhou, H.P.; Lu, Z.; Zhao, C.H.; Yang, X.L. Effect of strain rate on microstructure evolution of a nickel-based superalloy during hot deformation. *Mater. Des.* **2015**, *80*, 51–62. [CrossRef]
42. Xie, B.; Zhang, B.; Ning, Y.; Fu, M.W. Mechanisms of DRX nucleation with grain boundary bulging and subgrain rotation during the hot working of nickel-based superalloys with columnar grains. *J. Alloys Compd.* **2019**, *786*, 636–647. [CrossRef]
43. Jia, D.; Sun, W.R.; Xu, D.S.; Liu, F. Dynamic recrystallization behavior of GH4169G alloy during hot compressive deformation. *J. Mater. Sci. Technol.* **2019**, *35*, 1851–1859. [CrossRef]
44. Guo, Q.M.; Li, D.F.; Peng, H.J.; Guo, S.L.; Hu, J.; Du, P. Nucleation mechanisms of dynamic recrystallization in Inconel 625 superalloy deformed with different strain rates. *Rare Met.* **2012**, *31*, 215–220. [CrossRef]

45. Kumar, N.; Owolabi, G.M.; Jayaganthan, R.; Goel, S. Correlation of fracture toughness with microstructural features for ultrafine-grained 6082 Al alloy. *Fatigue Fract. Eng. Mater. Struct.* **2018**, *41*, 1884–1899. [CrossRef]
46. Liu, J.; Zhang, W.; Xin, X.; Wang, L.; Zhu, C.; Zhu, X.; Sun, W. Microstructure evolution and dynamic recrystallisation behaviour in hot deformation of Haynes 214 superalloy. *J. Alloys Compd.* **2022**, *919*, 165755. [CrossRef]
47. Wang, K.; Wen, D.; Li, J.; Zheng, Z.; Xiong, Y. Hot deformation behaviors of low-alloyed ultrahigh strength steel 30CrMnSiNi2A: Microstructure evolution and constitutive modeling. *Mater. Today Commun.* **2021**, *26*, 102009. [CrossRef]
48. Sakai, T.; Belyakov, A.; Kaibyshev, R.; Miura, H.; Jonas, J.J. Dynamic and post-dynamic recrystallization under hot, cold and severe plastic deformation conditions. *Prog. Mater. Sci.* **2014**, *60*, 130–207. [CrossRef]
49. Gourdet, S.; Montheillet, F. A model of continuous dynamic recrystallization. *Acta Mater.* **2003**, *51*, 2685–2699. [CrossRef]
50. Lin, Y.C.; Wu, X.-Y.; Chen, X.-M.; Chen, J.; Wen, D.-X.; Zhang, J.-L.; Li, L.-T. EBSD study of a hot deformed nickel-based superalloy. *J. Alloys Compd.* **2015**, *640*, 101–113. [CrossRef]
51. Yang, J.; Luo, J.; Li, X.; Li, M. Evolution mechanisms of recrystallized grains and twins during isothermal compression and subsequent solution treatment of GH4586 superalloy. *J. Alloys Compd.* **2021**, *850*, 156732. [CrossRef]

Disclaimer/Publisher's Note: The statements, opinions and data contained in all publications are solely those of the individual author(s) and contributor(s) and not of MDPI and/or the editor(s). MDPI and/or the editor(s) disclaim responsibility for any injury to people or property resulting from any ideas, methods, instructions or products referred to in the content.